

**(Fe,Co)<sub>2</sub>(P,Si) rare-earth free permanent magnets  
From macroscopic single crystals to submicron-sized particles**

Yibole, H.; Lingling-Bao, B.; Xu, J. Y.; Alata, H.; Tegus, O.; Hanggai, W.; van Dijk, N. H.; Brück, E.; Guillou, F.

**DOI**

[10.1016/j.actamat.2021.117388](https://doi.org/10.1016/j.actamat.2021.117388)

**Publication date**

2021

**Document Version**

Accepted author manuscript

**Published in**

Acta Materialia

**Citation (APA)**

Yibole, H., Lingling-Bao, B., Xu, J. Y., Alata, H., Tegus, O., Hanggai, W., van Dijk, N. H., Brück, E., & Guillou, F. (2021). (Fe,Co)<sub>2</sub>(P,Si) rare-earth free permanent magnets: From macroscopic single crystals to submicron-sized particles. *Acta Materialia*, 221, Article 117388. <https://doi.org/10.1016/j.actamat.2021.117388>

**Important note**

To cite this publication, please use the final published version (if applicable).  
Please check the document version above.

**Copyright**

Other than for strictly personal use, it is not permitted to download, forward or distribute the text or part of it, without the consent of the author(s) and/or copyright holder(s), unless the work is under an open content license such as Creative Commons.

**Takedown policy**

Please contact us and provide details if you believe this document breaches copyrights.  
We will remove access to the work immediately and investigate your claim.



25 properties can be achieved in  $(\text{Fe,Co})_2(\text{P,Si})$  quaternary alloys. This work correlates the  
26 development of permanent magnetic properties to a control of the microstructure. It paves the  
27 way toward the realization of permanent magnetic properties in  $(\text{Fe,Co})_2(\text{P,Si})$  alloys made of  
28 economically competitive Fe, P and Si elements, making these materials desirable for  
29 applications.

30 **Keywords:** Magnetism, Magnetic properties, Single crystal, Nanomaterials.

## 31        **1. Introduction**

32        Permanent magnets have become indispensable components of many mass-market consumer  
33        and industrial products, including applications in motors, generators and actuators. Nowadays,  
34        two families of magnets are produced on a large scale. The ferrite family, with the most common  
35        phases being  $\text{BaFe}_{12}\text{O}_{19}$  and  $\text{SrFe}_{12}\text{O}_{19}$ , are cheap and relatively easy to produce magnets, but  
36        their figure of merit, the energy product  $|BH|_{\text{max}}$  is limited, of the order of  $44 \text{ kJ m}^{-3}$ . On the other  
37        hand, rare-earth permanent magnets are high-performance magnets and represent about 2/3 of  
38        the permanent magnet market in monetary value [1]. The most well-known are Nd-Fe-B magnets,  
39        which can present energy products as high as  $500 \text{ kJ m}^{-3}$ . Nd-Fe-B is a very high-performance  
40        magnet, as it is largely made of iron and appropriate magnetic hysteresis can be maintained at  
41        temperatures up to  $200 \text{ }^\circ\text{C}$  by replacing Nd by heavy rare earths, Dy or Tb. Unfortunately, the  
42        criticality of the supply of heavy rare earths forces attention to be paid to the possibilities of  
43        replacing, or at least reducing the cost production and recycling of these magnets [2-5]. Therefore,  
44        developing new, cost-competitive, rare-earth-free materials with a maximum energy product lying  
45        in the gap between ferrite and rare-earth magnets is of primary importance [4]. Such a material  
46        could enhance the performance and reduce the weight of devices that currently use ferrites, or  
47        greatly reduce the cost of devices that currently use rare-earth magnets. Several 3d transition  
48        metal based materials families are considered as potential rare-earth-free permanent magnets,  
49        including MnBi, MnAl,  $\text{Mn}_2\text{Ga}$ ,  $\text{Fe}_{16}\text{N}_2$ ,  $\text{YCo}_5$ , FePt, CoPt [3-6]. But, despite intense research and  
50        the achievement of interesting properties, no clear preferred candidate emerges at present.

51        In this context the  $\text{Fe}_2\text{P}$  materials family is worth considering. The parent binary alloy is made by  
52        nearly 80 wt.% of iron, the most abundant magnetic element on earth, ensuring easy supply and  
53        a reasonable cost.  $\text{Fe}_2\text{P}$  also presents a reasonably large saturation magnetic polarization ( $J_s =$   
54         $\mu_0 M_s \approx 1.05 \text{ T}$  at 5 K) and a uniaxial magnetic anisotropy with the hexagonal  $c$  axis being the easy  
55        magnetic axis [7-9]. These later two properties are essential in view of realizing permanent

56 magnets. Its magneto-crystalline anisotropy energy is particularly large, stronger than most of the  
57  $3d$  based alloys mentioned above. However, its low Curie temperature of  $T_C = 214$  K is  
58 incompatible with applications. By substitution of Fe by Co, De Vos *et al.* reported in 1962 an  
59 increase in Curie temperature and the possibility to prepare permanent magnets with a coercive  
60 field  $\mu_0 H_c$  of about 0.2 T at room temperature [10]. Further attempts at developing permanent  
61 magnets deriving from  $Fe_2P$  have however been impeded by the appearance of a competing  
62 orthorhombic crystal structure in  $Fe_{2-y}Co_yP$  ternary alloys when  $y$  reaches 0.3 [11]. Substituting Ni  
63 for Fe is also known to increase the Curie temperature, but at the expense of a reduction in both  
64 magnetic anisotropy and saturation magnetization [12]. Similarly, substitutions of P for other  
65 metalloid such as Si, As, Ge, or B raise  $T_C$ , but also result in the appearance of competing crystal  
66 structures [13-15]. At the end, it turned out difficult to optimize ternary alloys deriving from  $Fe_2P$   
67 for permanent magnet applications. Even though significant advances have been made to  
68 prepare  $Fe_{2-y}Co_yP$  in nanosized form, the relatively large coercive field of  $\mu_0 H_c = 0.57$  T at 5 K of  
69 such small nanoparticles quickly vanishes as the blocking temperature of these  
70 superparamagnetic particles is relatively low [16-19].

71 Several theoretical studies have clarified the origin of the large magneto-crystalline anisotropy in  
72  $Fe_2P$  and related alloys, which in particular highlighted the strong dependence of the magnetic  
73 properties on both the band filling and structural distortions affecting the  $c/a$  ratio of the hexagonal  
74 lattice parameters [20,21]. It led to the prediction of the possibility to maintain a strong magneto-  
75 crystalline anisotropy of  $Fe_2P$  in quaternary alloys by simultaneous substitutions on the metal and  
76 metalloid sites [22]. Yet more experimental insights are needed, in particular as the stability range  
77 of the hexagonal structure is virtually unknown in quaternary alloys deriving from  $Fe_2P$ , except for  
78  $(Mn,Fe)_2(P,As)$ ,  $(Mn,Fe)_2(P,Ge)$  or  $(Mn,Fe)_2(P,Si)$  studied for their giant magnetocaloric effect [23-  
79 26]. Preliminary experimental studies in polycrystalline  $Fe_{2-y}Co_yP_{1-x}Si_x$  and  $Fe_{2-y}Ni_yP_{1-x}Si_x$  allowed  
80 us to roughly estimate the chemical compositions for which the hexagonal  $Fe_2P$ -type structure

81 can be observed, and an oriented powder method suggested the possibility to combine high Curie  
82 temperatures and strong magnetic anisotropy with *c* as easy axis [27,28]. However, two main  
83 issues remained to be tackled, prior to quaternary compounds deriving from Fe<sub>2</sub>P could be truly  
84 considered as potential rare-earth-free permanent magnets. First, a more accurate determination  
85 of the magneto-crystalline anisotropy constants than that obtained in oriented Fe<sub>2-y</sub>Co<sub>y</sub>P<sub>1-x</sub>Si<sub>x</sub>  
86 polycrystalline materials is needed. Ideally, this requires single crystals. While the growth of binary  
87 Fe<sub>2</sub>P and ternary Fe<sub>2-y</sub>Ni<sub>y</sub>P single crystals has been reported a few decades ago [7,12], that of  
88 quaternary alloys containing Si is highly challenging due to the combination of a high volatility of  
89 P and a low solubility of Si in the flux. The growth of ferromagnetic quaternary alloys deriving from  
90 Fe<sub>2</sub>P has seldom been successful; So far, only in Fe<sub>2-y</sub>Mn<sub>y</sub>P<sub>1-x</sub>Si<sub>x</sub> magnetocaloric materials with  
91 low *T<sub>C</sub>* or with antiferromagnetic order, *i.e.* with a limited Si content [29]. The second aspect  
92 requiring attention is that Fe<sub>2-y</sub>Co<sub>y</sub>P<sub>1-x</sub>Si<sub>x</sub> polycrystalline materials do not show coercivity nor  
93 remanence in bulk form after synthesis by solid state reaction. As demonstrated here, developing  
94 appropriate microstructures is beneficial to turn the large magnetic anisotropy into true hard  
95 magnetic properties.

## 96 **2. Experimental Methods**

### 97 **2.1 Single crystals synthesis**

98 Fe<sub>2-y</sub>Co<sub>y</sub>P and Fe<sub>2-y</sub>Co<sub>y</sub>P<sub>1-x</sub>Si<sub>x</sub> single crystals were grown by the flux method with tin as a metallic  
99 flux. Several batches were synthesized to obtain the targeted Co and Si compositions. High-purity  
100 Co (99.9%), Fe (99.9%), P (97.3%), and Si (99.999%) were used as starting materials. The  
101 starting materials were mixed with high-purity Sn (99.99%) and then arc-melted under an Ar  
102 atmosphere in water-cooled copper crucible. The resulting ingot was then sealed in a quartz  
103 ampoule in an Ar atmosphere of 200 mbar. The charge to flux ratio was 1:20 wt. %. The sealed  
104 ampoules were placed in a vertical furnace and heated to 1473 K over 10 h, then maintained at  
105 this temperature for 100 h, and later cooled at a rate of 2.5 K h<sup>-1</sup> to 900 K at which temperature

106 the excess of tin was removed. The remaining flux was removed by etching with diluted  
107 hydrochloric acid.

## 108 **2.2 Submicron-sized particles synthesis**

109  $\text{Fe}_{1.75}\text{Co}_{0.20}\text{P}_{0.8}\text{Si}_{0.2}$  submicron-sized particles were produced by a two-stage process. First, bulk  
110 polycrystalline materials are prepared by mechanical alloying (planetary Fritsch Pulverisette) of  
111 elemental starting materials during 10 h using a ball:sample weight ratio of 5:1 followed by shaping  
112 into pellet and a solid state reaction at 1100 °C during 24 h ending by a quenching. The resulting  
113 bulk polycrystalline samples mainly consist of the main  $\text{Fe}_2\text{P}$ -type phase (about 95 wt.%, with  
114 some contamination from secondary phase having 3:1 or 5:3 metal:metalloid ratio depending on  
115 Si content) and are well crystallized with an average grain size of the order of 40  $\mu\text{m}$ . At the  
116 second step, submicron-sized particles are produced by ball-milling (ball:sample mass ratio 6:1  
117 in stainless steel jars with balls of 4 g) either using dry milling or surfactant assisted wet milling  
118 with Heptane (99.8% purity) as solvent with 20 wt.% oleic acid (90 % purity) as surfactant. The  
119 jars were sealed under purified Ar atmosphere. Different milling times were used.

## 120 **2.3 Chemical and physical characterizations**

121 The morphology and chemical composition of the single crystal were determined by scanning  
122 electron microscopy (SEM, Hitachi SU8010 and Hitachi TM3030Plus) and energy-dispersive  
123 X-ray spectroscopy (EDS, using an acceleration voltage of 15 keV). To get a more quantitative  
124 estimate of chemical compositions, polycrystalline  $\text{Fe}_{1.00}\text{Si}_{1.00}$  and monocrystalline  $\text{Fe}_{2.00}\text{P}_{1.00}$   
125 references were used.

126 An Empyrean PANalytical diffractometer employing Cu-K radiation was used for powder x-ray  
127 diffraction with the internal parameters of the PIXcel detector adjusted to reduce the fluorescence  
128 background. For polycrystalline materials, structural refinements were carried out using the

129 Rietveld method and Fullprof software to confirm the phase content [30]. The VESTA software  
130 was used for structure visualization [31].

131 Magnetic measurements were carried out using a Quantum Design Versalab system equipped  
132 with a vibrating sample magnetometer option. For calculation of the anisotropy constant, the  
133 demagnetizing field was corrected assuming the internal field  $H_{in} = H_0 - NM$ , where  $H_0$  is the applied  
134 field,  $M$  the volume magnetization and  $N$  the demagnetizing factor calculated for each crystal  
135 using the Osborn tables. In practice the demagnetizing field correction is mostly needed for  
136 measurements with the applied field perpendicular to the long axis of the crystal as the  
137 demagnetizing factor in this configuration are of the order of 0.45-0.47, close to the value of  $N =$   
138  $1/2$  expected for an infinitively long needle. For magnetic measurements above 400 K a  
139 Lakeshore 7407 vibrating sample magnetometer was used in combination with an electromagnet  
140 and a high temperature furnace model 74034 using BN crucibles.

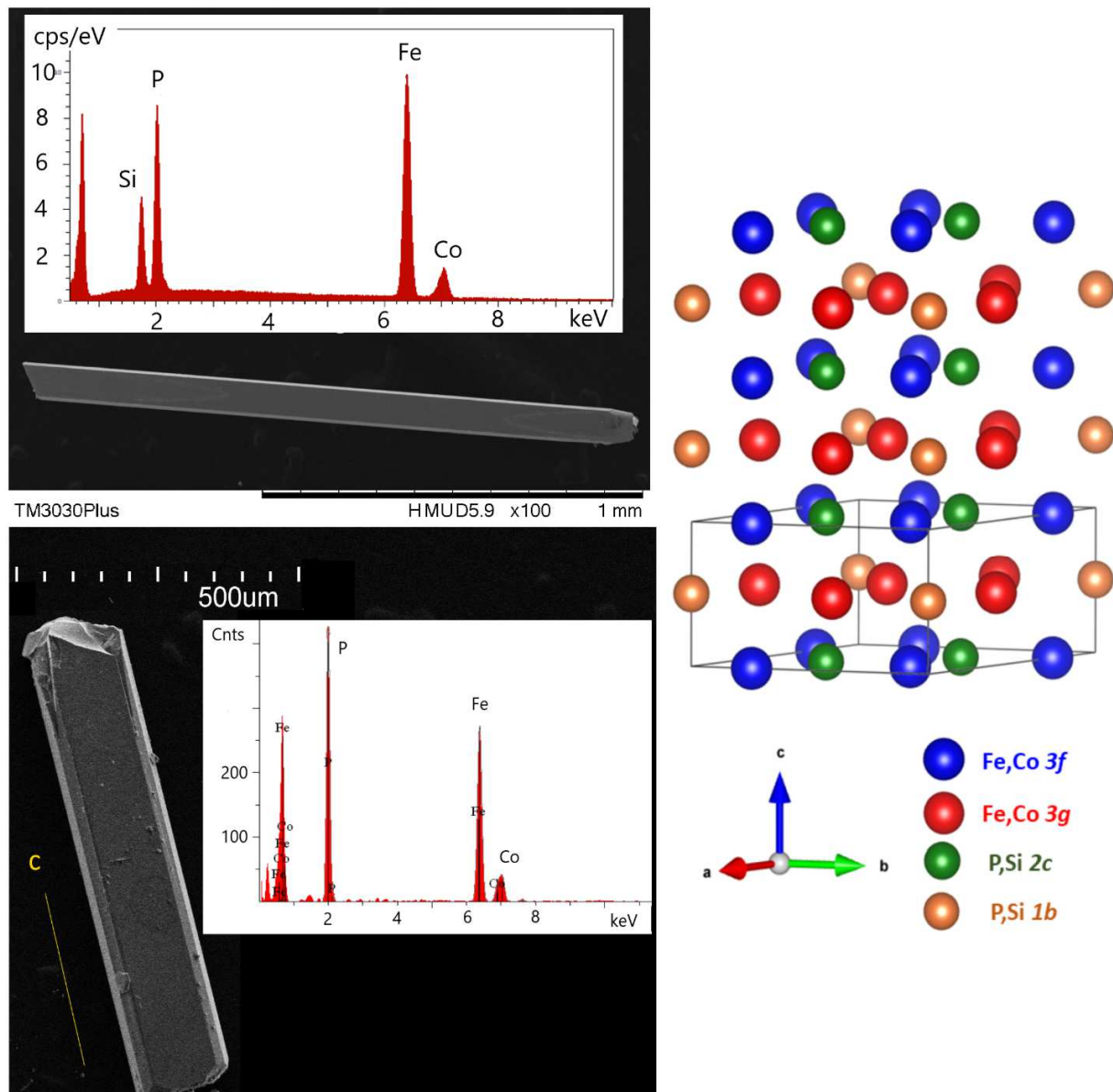
### 141 **3. Results and discussion**

#### 142 **3.1 Growth of $Fe_{2-y}Co_yP_{1-x}Si_x$ single crystals**

143 Several batches of  $Fe_{2-y}Co_yP_{1-x}Si_x$  single crystals were grown with a focus on the composition  
144 range  $0.1 \leq y \leq 0.5$  and  $0.2 \leq x \leq 0.4$ , respectively. From our preliminary study on polycrystalline  
145 samples these compositions appeared the most likely to yield a high  $T_C$  and a strong magnetic  
146 anisotropy [27]. Simultaneous Co for Fe and Si for P substitutions are required to ensure that the  
147 crystal structure is of the hexagonal  $Fe_2P$ -type at large Si content, the latter being essential to  
148 reach high Curie temperatures. Ternary  $(Fe,Co)_2P$  single crystals were also grown to serve as  
149 comparative examples. As the flux growth method leads to a certain dispersion of the crystal  
150 compositions with respect to the nominal ones, the compositions of the crystals were  
151 systematically established using scanning electron microscopy (SEM) coupled with energy  
152 dispersive X-ray spectroscopy (EDS) assisted by appropriate references. **Figure 1** presents two



153 typical crystals: a quaternary  $\text{Fe}_{1.94\pm 0.06}\text{Co}_{0.10\pm 0.01}\text{P}_{0.61\pm 0.02}\text{Si}_{0.33\pm 0.01}$  and a ternary  
154  $\text{Fe}_{1.78\pm 0.04}\text{Co}_{0.23\pm 0.01}\text{P}_{0.98\pm 0.02}$  crystal. Both crystals have a prismatic elongated needle-like shape  
155 similar to the shape previously observed in hexagonal  $\text{MnFe}(\text{P},\text{Si})$  single crystals [29]. The  
156 surfaces of the crystals are regular and of homogeneous composition. The ternary crystal has  
157 dimensions of about  $0.13\times 0.13\times 0.8\text{ mm}^3$  and its chemical composition  $\text{Fe}_{1.78}\text{Co}_{0.23}\text{P}_{0.98}$  is close to  
158 the nominal starting composition  $\text{Fe}_{1.80}\text{Co}_{0.20}\text{P}$ . The quaternary crystal has average dimensions  
159 of about  $1.50\times 0.07\times 0.07\text{ mm}^3$ . The analysis of the EDS spectrum indicates a metal:metalloid ratio  
160 of about 2.17:1. This is larger than, yet close to 2:1 (nominal starting composition  
161  $\text{Fe}_{1.90}\text{Co}_{0.10}\text{P}_{0.5}\text{Si}_{0.65}$ ) and significantly different from the other alloys eventually forming, usually  
162 having 5:3 or 3:1 for the metal:metalloid ratio [27]. Growing crystals of quaternary compounds  
163 containing Si therefore turned out more complex than for ternary. Due to the poor solubility of Si  
164 in molten tin and the facilitated formation of secondary phases close to  $\text{Fe}_5\text{Si}_3$  or  $\text{Fe}_3\text{Si}$ , the growth  
165 of  $\text{Fe}_{2-y}\text{Co}_y\text{P}_{1-x}\text{Si}_x$  crystals is challenging and the outcome difficult to anticipate. Starting from a  
166 nominal composition leads to collecting a large variety of crystals with a broad range of  
167 compositions. Only a few of them present a metal:metalloid ratio close to 2:1 and a needle shape  
168 expected for materials having a hexagonal structure. Additional batches of  $\text{Fe}_{2-y}\text{Co}_y\text{P}_{1-x}\text{Si}_x$  crystals  
169 were prepared to cover the targeted composition range, as for the Co-rich  
170  $\text{Fe}_{1.50\pm 0.03}\text{Co}_{0.50\pm 0.02}\text{P}_{0.70\pm 0.02}\text{Si}_{0.30\pm 0.01}$  crystal ( $\text{Fe}_{1.75}\text{Co}_{0.25}\text{P}_{0.45}\text{Si}_{0.65}$  starting composition) presented  
171 hereafter.



172

173

174

175

176

177

178

**Figure 1.** SEM images of as-grown  $\text{Fe}_{1.94\pm 0.06}\text{Co}_{0.10\pm 0.01}\text{P}_{0.61\pm 0.02}\text{Si}_{0.33\pm 0.01}$  (top) and  $\text{Fe}_{1.78\pm 0.04}\text{Co}_{0.23\pm 0.01}\text{P}_{0.98\pm 0.02}$  (bottom) single crystals. The insets illustrate the corresponding chemical analysis by EDS. On the right, crystal structure representation of hexagonal  $(\text{Fe,Co})_2(\text{P,Si})$  alloys. The basic unit cell (solid contour) was tripled along the *c* direction to highlight the stacking of layers containing inequivalent *3f* and *3g* metal sites along the *c* axis.

179

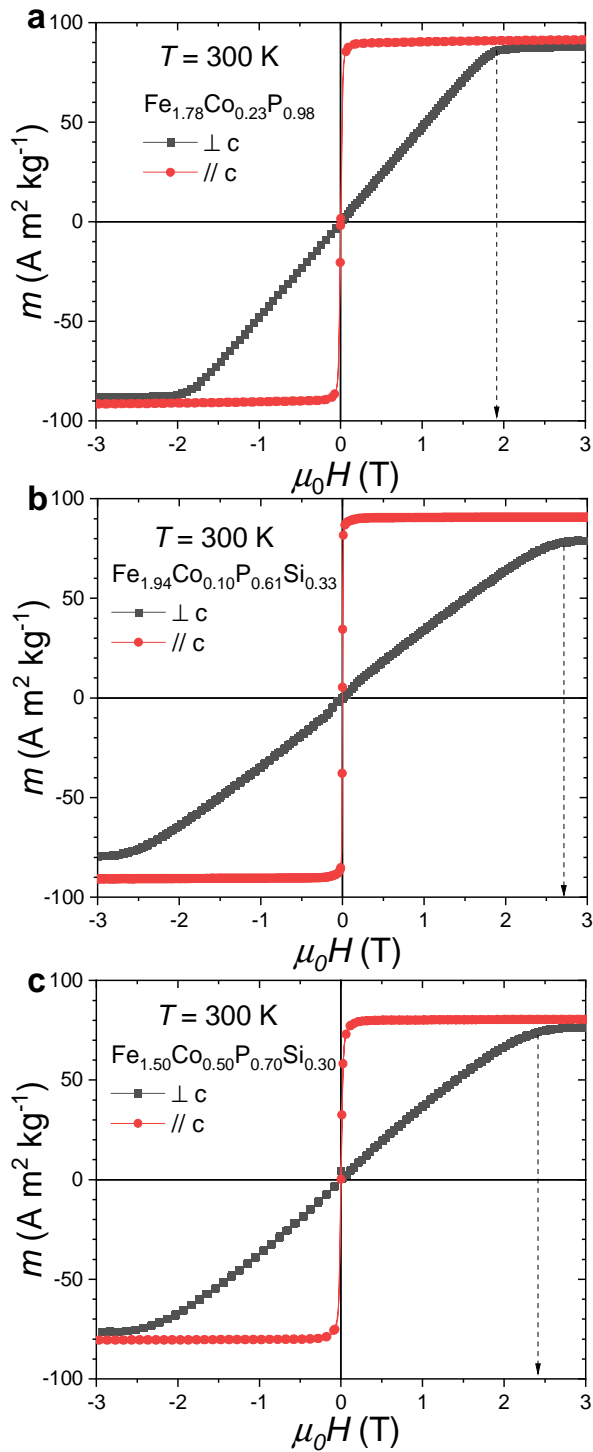
### 180 **3.2 Large magnetocrystalline anisotropy in $\text{Fe}_{2-y}\text{Co}_y\text{P}_{1-x}\text{Si}_x$ single crystals**

181 In order to highlight the interest in quaternary  $\text{Fe}_{2-y}\text{Co}_y\text{P}_{1-x}\text{Si}_x$  compounds in comparison to binary  
182  $\text{Fe}_2\text{P}$  or ternary  $(\text{Fe},\text{Co})_2\text{P}$ , we selected three representative crystals for the exploration of the  
183 magnetic properties. First, the ternary  $\text{Fe}_{1.78}\text{Co}_{0.23}\text{P}_{0.98}$  crystal serves as comparative example  
184 illustrating the influence of Co for Fe substitution in  $\text{Fe}_2\text{P}$ . We recall that this composition is one  
185 of the highest Co contents achievable prior to the appearance of the orthorhombic structure in  
186 ternary  $(\text{Fe},\text{Co})_2\text{P}$  [11]. The second crystal  $\text{Fe}_{1.94}\text{Co}_{0.10}\text{P}_{0.61}\text{Si}_{0.33}$  is a quaternary sample with  
187 limited Co for Fe and Si for P substitutions. The third  $\text{Fe}_{1.50}\text{Co}_{0.50}\text{P}_{0.70}\text{Si}_{0.30}$  crystal illustrates the  
188 properties of quaternary compounds with a higher Co content.

189 **Figure 2** presents the magnetization curves of the three crystals at room temperature ( $T = 300$  K)  
190 recorded parallel and perpendicular to the long axis of the needle, which is the crystallographic  $c$   
191 axis. We first note that no significant hysteresis can be distinguished between magnetization and  
192 demagnetization curves of the present single crystals. Then, even though the uncertainty in the  
193 normalized magnetization is relatively large (of the order of 10%), as relying on volume of crystals  
194 estimated from SEM, Co for Fe substitution appears to trigger a reduction in magnetization at high  
195 Co content. The room temperature data for  $\text{Fe}_{1.50}\text{Co}_{0.50}\text{P}_{0.70}\text{Si}_{0.30}$  presents a specific saturation  
196 magnetization that is approximately  $10 \text{ A m}^2 \text{ kg}^{-1}$  lower than that of  $\text{Fe}_{1.94}\text{Co}_{0.10}\text{P}_{0.61}\text{Si}_{0.33}$ . Similarly,  
197 the low temperature data ( $T = 50$  K, Supplementary Material), indicate that the specific saturation  
198 magnetization of  $\text{Fe}_{1.78}\text{Co}_{0.23}\text{P}_{0.98}$  was found to be  $m_s \approx 122 \text{ A m}^2 \text{ kg}^{-1}$  ( $J_s \approx 1.06$  T), which is  
199 comparable to that of the binary  $\text{Fe}_2\text{P}$  parent. However, larger Co content and Si substitutions  
200 trigger a reduction in saturation specific magnetization down to  $\sim 90 \text{ A m}^2 \text{ kg}^{-1}$  ( $J_s \approx 0.81$  T) for  
201  $\text{Fe}_{1.50}\text{Co}_{0.50}\text{P}_{0.70}\text{Si}_{0.30}$  at 50 K. In addition, the magnetization saturates to lower values when  
202 measured along the hard  $c$  axis magnetic direction than perpendicular to it. This anisotropy of the  
203 saturation magnetization is pronounced at room temperature for the  $\text{Fe}_{1.94}\text{Co}_{0.10}\text{P}_{0.61}\text{Si}_{0.33}$  crystal

204 showing the strongest anisotropy prior saturation (approximately 10% at  $\mu_0 H = 3$  T). A significant  
205 anisotropy of the magnetization (~9%) was also reported for the parent Fe<sub>2</sub>P composition at 5 K  
206 [9], though a smaller anisotropy (~2%) was found for MnFe(P,Si) with the *c* axis as the easy  
207 magnetic axis [29]. The anisotropy of the magnetization appears particularly large in Fe<sub>2</sub>P-type  
208 materials, in particular in comparison to other 3*d* metals (usually considered of the order of ~0.1%  
209 in Co [32]), and would deserve a dedicated study.

210 More interesting for applicative purposes is the large magnetic anisotropy before saturation –even  
211 at room temperature– exhibited by the three crystals when comparative measurements were  
212 performed parallel and perpendicular to the *c* crystallographic axis. In these three cases, the  
213 anisotropy fields ( $\mu_0 H_A$ ) are of the order of 2 to 3 T. Yet, we can observe significant differences  
214 between the three samples. At room temperature, the two quaternary compounds present a  
215 significantly larger anisotropy field than the ternary Fe<sub>1.78</sub>Co<sub>0.23</sub>P<sub>0.98</sub> crystal. This provides a direct  
216 confirmation that simultaneous substitutions of Co for Fe and Si for P enables a large magneto-  
217 crystalline anisotropy at room temperature in materials deriving from Fe<sub>2</sub>P. In addition, the  
218 anisotropy field  $\mu_0 H_A$  of about 2.8 T for Fe<sub>1.94</sub>Co<sub>0.10</sub>P<sub>0.61</sub>Si<sub>0.33</sub> is larger than that of the  
219 Fe<sub>1.50</sub>Co<sub>0.50</sub>P<sub>0.70</sub>Si<sub>0.30</sub> crystal with a higher Co content ( $\mu_0 H_A \approx 2.5$  T). This reveals the existence of  
220 optimal Co and Si contents that maximize the anisotropy field at room temperature, as previously  
221 suggested on the basis of theoretical calculations and polycrystalline data [22,27].

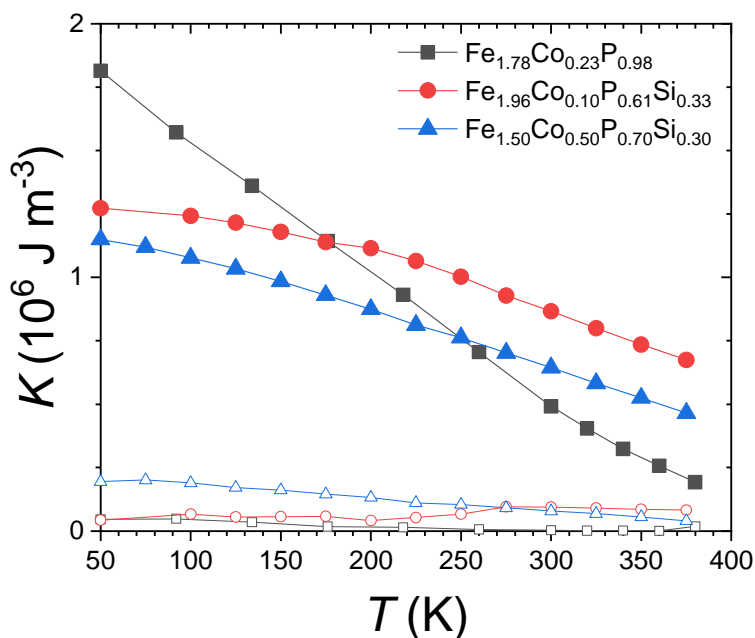


222

223 **Figure 2.** Specific magnetization curves for three  $\text{Fe}_{2-y}\text{Co}_y\text{P}_{1-x}\text{Si}_x$  single crystals measured  
 224 parallel and perpendicular to the  $c$  axis at room temperature ( $T = 300$  K) upon magnetizing and  
 225 demagnetizing.

226 To obtain more quantitative information characterizing the magnetic anisotropy, we turn now  
 227 toward the first- ( $K_1$ ) and second-order ( $K_2$ ) anisotropy constants that define the magneto-  
 228 crystalline anisotropy energy of a hexagonal system,  $E \approx K_1 \sin^2 \theta + K_2 \sin^4 \theta$ , where  $\theta$  is the angle  
 229 between the direction of the magnetization and the hexagonal  $c$  axis. The Sucksmith and  
 230 Thompson method was used to determine  $K_1$  and  $K_2$  from magnetization curves recorded parallel  
 231 and perpendicular to the  $c$  direction in the temperature range of 50 - 375 K [33]. **Figure 3** shows  
 232 the temperature dependence of the anisotropy constants for the three crystals. As expected for  
 233 materials having an easy  $c$  axis magnetic anisotropy,  $K_1$  is positive and largely dominant in all  
 234 three crystals. In this case an alternative estimate of  $K_1$  can be made from the anisotropy field  
 235 and the saturation magnetization ( $M_S$ ) by neglecting  $K_2$ , resulting in  $K_1 \approx \mu_0 H_A M_S / 2$  [6]. This  
 236 alternative method for instance leads to  $K_1 \approx 0.9 \text{ MJ m}^{-3}$  for  $\text{Fe}_{1.94}\text{Co}_{0.10}\text{P}_{0.61}\text{Si}_{0.33}$  at room  
 237 temperature, which is in good agreement with the Sucksmith and Thompson method ( $K_1 \approx 0.87$   
 238  $\text{MJ m}^{-3}$  and  $K_2 \approx 0.09 \text{ MJ m}^{-3}$ ). We also note that the present anisotropy constants of single crystals  
 239 provide a confirmation for former quantitative estimate from oriented powder samples ( $K_1 \approx 0.93$   
 240  $\text{MJ m}^{-3}$  in a closely related  $\text{Fe}_{1.75}\text{Co}_{0.20}\text{P}_{0.80}\text{Si}_{0.20}$  composition [27]) and for theoretical calculations  
 241 ( $K \approx 0.2 \text{ meV f.u.}^{-1}$  ( $0.96 \text{ MJ m}^{-3}$ ) around room temperature for a composition close to  
 242  $\text{Fe}_{1.88}\text{Co}_{0.12}\text{P}_{0.76}\text{Si}_{0.24}$ ) [22]. At room temperature, the largest magneto-crystalline anisotropy is  
 243 observed for the  $\text{Fe}_{1.94}\text{Co}_{0.10}\text{P}_{0.61}\text{Si}_{0.33}$  crystal. At 50 K, the largest anisotropy is found in the ternary  
 244  $\text{Fe}_{1.78}\text{Co}_{0.23}\text{P}_{0.98}$  crystal with  $K_1 \approx 1.81 \text{ MJ m}^{-3}$  ( $K_1 \approx 2.03 \text{ MJ m}^{-3}$  at 5 K) which is a very sizable  
 245 value for a transition-metal based compounds, yet smaller than the  $\text{Fe}_2\text{P}$  binary parent (2.4-2.9  
 246  $\text{MJ m}^{-3}$ ) [9]. In hexagonal symmetry,  $K_1$  is usually considered to scale as  $M_S^3(T)$  at low temperature  
 247 and as  $(3/5)M_S^2(T)$  near  $T_C$  [6,34], which primarily explains that in  $\text{Fe}_{1.78}\text{Co}_{0.23}\text{P}_{0.98}$  the magnetic  
 248 anisotropy decreases much faster with the temperature than the magnetization and that Curie  
 249 temperatures much higher than room temperature are required to reach a large room-temperature  
 250 anisotropy, as achieved in  $(\text{Fe,Co})_2(\text{P,Si})$  quaternary alloys. These tendencies allow one to draw  
 251 the following scenario on the evolution of the magnetic properties as function of chemical

252 substitutions. The binary parent is likely to be close to the optimum to maximize the magnetic  
 253 anisotropy at low temperature. Co for Fe and Si for P substitutions increase the Curie temperature,  
 254 but decrease the ground state magneto-crystalline anisotropy, therefore requiring to mitigate both  
 255 aspects to reach a large magnetic anisotropy at room temperature. This is also the primary reason  
 256 why the maximum room-temperature magnetic anisotropy was observed at relatively limited  
 257 substitutions with Co around 0.2 and Si between 0.2 to 0.25 in the preliminary polycrystalline data  
 258 [27].



259  
 260 **Figure 3.** Magneto-crystalline anisotropy constants  $K_1$  (full symbols) and  $K_2$  (open symbols)  
 261 determined as a function of the temperature by the Sucksmith and Thompson method for the  
 262 three single crystals.

263 **Table 1** summarizes the magnetic anisotropy parameters of the three crystals and compares it to  
 264 some candidate rare-earth-free permanent magnets.  $(\text{Fe,Co})_2(\text{P,Si})$  materials present a  
 265 significantly larger magnetic anisotropy and saturation magnetization than ferrites. The  
 266 magnetocrystalline anisotropy of  $(\text{Fe,Co})_2(\text{P,Si})$  remains lower than  $L_{10}$  CoPt or FePt permanent

267 magnet candidates, but Pt containing materials are not economically competitive compared to  
268 other magnets, even for rare-earth magnets.  $(\text{Fe,Co})_2(\text{P,Si})$  present a magnetocrystalline  
269 anisotropy and a saturation magnetization that is comparable to the best Mn-based candidates  
270 for rare-earth-free permanent magnets. The magnetic hardness parameter  $\kappa = \sqrt{(K_1/\mu_0 M_S^2)}$  is a  
271 convenient figure of merits for permanent magnets, with  $\kappa > 1$  the threshold for a material to resist  
272 to self-demagnetization [6,35]. The room-temperature magnetic hardness parameters for ternary  
273  $(\text{Fe,Co})_2\text{P}$  and quaternary  $(\text{Fe,Co})_2(\text{P,Si})$  alloys are about 1.0 and 1.3, respectively. This further  
274 supports that these materials are potential hard magnetic materials, and the larger  $\kappa$  for  
275 quaternaries highlights their increased interest compared to the ternary alloys. Overall, by  
276 combining a high Curie temperature, a large magnetic anisotropy and a relatively large saturation  
277 magnetization, the  $(\text{Fe,Co})_2(\text{P,Si})$  system is highly promising for permanent magnet applications  
278 and would suitably fit in the performance gap between ferrites and rare-earth magnets.

279



280 **Table 1.** Comparison of the main anisotropy constant ( $K$ ), saturation specific magnetization  
 281 ( $m_s$ ), saturation magnetic polarization ( $J_s$ ), magnetic hardness parameter ( $\kappa$ , calculated for the  
 282 present samples using anisotropy constants and saturation magnetizations at 300 K), and  
 283 magnetic transition temperature ( $T_{tr}$ ) between the present crystals, representative ferrites and  
 284 some rare-earth-free permanent magnet candidates.

Material	$K$ (50 K)	$K$ (300 K)	$m_s$ (50 K)	$J_s$	$\kappa$ (300 K)	$T_{tr}$	Ref.
	[MJ m <sup>-3</sup> ]	[MJ m <sup>-3</sup> ]	[A m <sup>2</sup> kg <sup>-1</sup> ]	[T]		[K]	
Fe <sub>1.78</sub> Co <sub>0.23</sub> P <sub>0.98</sub>	1.81	0.50	122	1.06 (50 K)	1.0	412	present
Fe <sub>1.94</sub> Co <sub>0.10</sub> P <sub>0.61</sub> Si <sub>0.33</sub>	1.28	0.87	101	0.88 (50 K)	1.3	560	present
Fe <sub>1.50</sub> Co <sub>0.50</sub> P <sub>0.70</sub> Si <sub>0.30</sub>	1.15	0.65	90	0.81 (50 K)	1.3	535	present
Fe <sub>2</sub> P	2.2	-	125	1.05 (50 K)	-	214	[7-9]
BaFe <sub>12</sub> O <sub>19</sub>	0.45	0.33	92	0.48	1.35	725	[35,36]
SrFe <sub>12</sub> O <sub>19</sub>	-	0.35	90	0.45	1.2	732	[35,37]
MnBi	-0.2	1.1	62	0.73	1.46	628	[35,38]
MnAl	1.7	1.2	110	0.75	1.95	620	[35,39]
CoPt	4.9	4.1	55	1.01	2.47	840	[35,40]
FePt	7.4	6.0	90	1.43	2.02	660	[6,41]

285

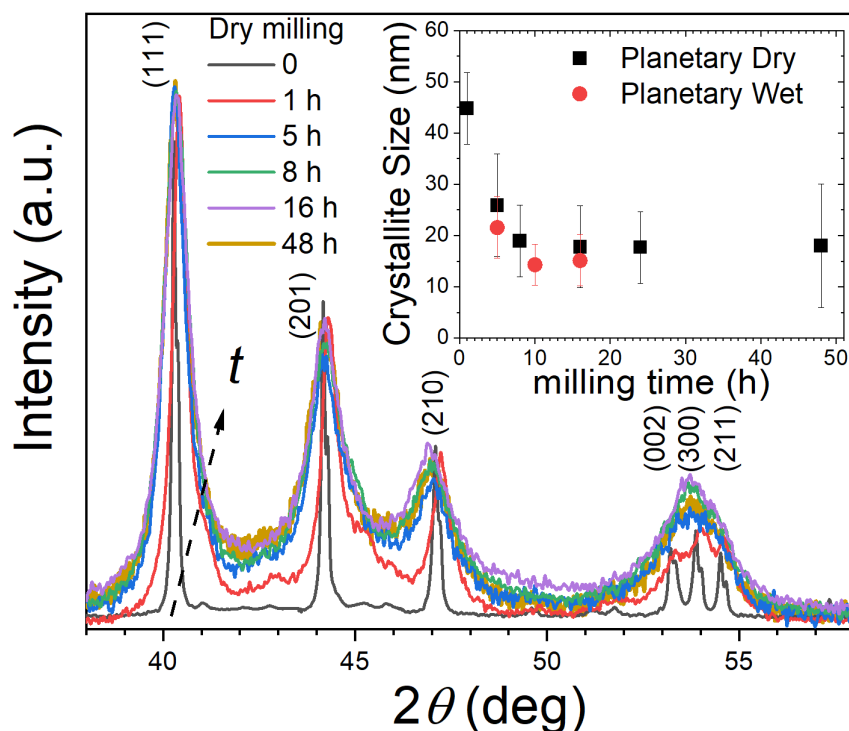
286

### 287 3.3 Top-down synthesis of $\text{Fe}_{2-y}\text{Co}_y\text{P}_{1-x}\text{Si}_x$ submicron-sized particles

288  $(\text{Fe,Co})_2(\text{P,Si})$  materials do not present significant coercive field in single crystals or bulk  
289 polycrystalline materials due to the formation of a magnetic multidomain configuration. One  
290 approach to induce hard magnetic properties can be to restore a single domain structure by  
291 reducing the particle size. The maximum single domain size for an isolated particle can be  
292 estimated as  $R_{\text{sd}} \approx 36(AK_1)^{1/2}/\mu_0 M_S^2 \approx 150$  nm, with  $A$  the exchange stiffness parameter, which is  
293 usually of the order of  $10 \text{ pJ m}^{-1}$  for transition metal ferromagnets with a Curie temperature well  
294 above room temperature [6]. This maximum single domain size is comparable to other permanent  
295 magnetic materials (about 270 nm in ferrites and 110 nm in  $\text{Nd}_2\text{Fe}_{14}\text{B}$ ) [6]. The smallest width of  
296 the stripes observed in MFM microscopy was about 200 nm (Supplemental Material Figure S3),  
297 which is comparable to the theoretical estimate. Both estimates indicate that the single domain  
298 size corresponds to the range of relatively large particles, which can be obtained by top down  
299 methods.  $\text{Fe}_{2-y}\text{Co}_y\text{P}_{1-x}\text{Si}_x$  submicron-sized particles were therefore synthesized by ball-milling of  
300 bulk polycrystalline samples. While ball-milling usually leads to the development of microstrains,  
301 crystallite agglomeration and results in irregular particle shapes of variable size, for this first  
302 exploration of  $(\text{Fe,Co})_2(\text{P,Si})$  particles it was the preferred method as it allows a good control of  
303 the chemical composition. Different milling methods were explored including vibratory ball-milling,  
304 dry planetary ball-milling and wet planetary ball-milling with surfactant. All these methods led to  
305 the synthesis of submicron-sized particles with an appreciable coercive field. We hereafter focus  
306 on presenting materials prepared by dry planetary ball-milling, as this method is the most  
307 straightforward to scale-up.

308 **Figure 4** presents powder X-ray diffraction patterns of  $\text{Fe}_{1.75}\text{Co}_{0.20}\text{P}_{0.75}\text{Si}_{0.25}$  submicron-sized  
309 particles prepared by ball milling of polycrystalline material. The starting polycrystalline material  
310 presents a diffraction pattern typical for the  $\text{Fe}_2\text{P}$ -type hexagonal crystal structure. A minor  
311 contamination from a secondary phase having a 5:3 metal:metalloid ratio can however be

312 distinguished (<4 wt.%). Increasing the milling time leads to a significant peak broadening up to  
313 8 h milling, then it saturates. The three most intense peaks of the Fe<sub>2</sub>P-type phase (111), (201)  
314 and (210) from 40.3° to 47.2° remain independent allowing an estimation of the crystallite size (*d*)  
315 using the Sherrer's equation  $d = k\lambda/\beta\cos\theta$ , where *k* is a constant that depends on the crystallite  
316 shape and the definition of an average diameter, usually taken as *k* = 0.9,  $\lambda$  is the X-ray  
317 wavelength, and  $\beta$  is the broadening of the (111) diffraction peak. Additional sources of peak  
318 broadening were not considered in first approximation. In particular, the development of  
319 (micro)strains was not accounted for since, at the exception of the (210) peak presenting a small  
320 shift to lower angles, no significant changes in peak positions could be observed. Ball milling leads  
321 to a progressive crystallite size reduction down to about 20 nm after 8 h of milling. Similar  
322 crystallite sizes were obtained when preparing submicrometric particles of MnFe(P,Si) giant  
323 magnetocaloric materials by ball milling [42]. Increasing the milling time further does not lead to  
324 a significant further reduction in crystallite size. Very long milling, e.g. 48 h, however results in the  
325 appearance of a broad bump around 18°, indicating the appearance of an amorphous phase.  
326 From the point of view of reaching a large coercive field without compromising the saturation  
327 magnetization by the formation of an amorphous phase, the optimal milling time is therefore  
328 expected to be in the range of 5 - 16 h. Using the same mill (planetary ball mill with same rotary  
329 milling speed, jars size and ball mass), but polycrystalline materials dispersed in heptane solvent  
330 with oleic acid surfactant (wet milling) results in similar crystallite sizes and magnetic coercivity.  
331 This indicates that the presently obtained crystallite size is partly limited by the milling energy. In  
332 addition, SEM imaging of the ball-milled product (Supplementary material) revealed a very broad  
333 particle size distribution ranging from crystallites of less than 100 nm up to 40  $\mu$ m particles formed  
334 by the agglomeration of (sub)micrometer-sized crystallites.



335

336 **Figure 4.** Structure  $\text{Fe}_{1.75}\text{Co}_{0.20}\text{P}_{0.75}\text{Si}_{0.25}$  submicron-sized particles. The X-ray diffraction  
 337 patterns of dry ball-milled  $\text{Fe}_{1.75}\text{Co}_{0.20}\text{P}_{0.75}\text{Si}_{0.25}$  powders with increasing milling times of 1, 5, 8,  
 338 16 and 48 h are compared to that of hand-crushed polycrystalline material. The patterns were  
 339 subtracted for background and normalized to highlight the peak broadening. The inset presents  
 340 the crystallite size estimated with the Sherrer's equation using the (111) reflection.

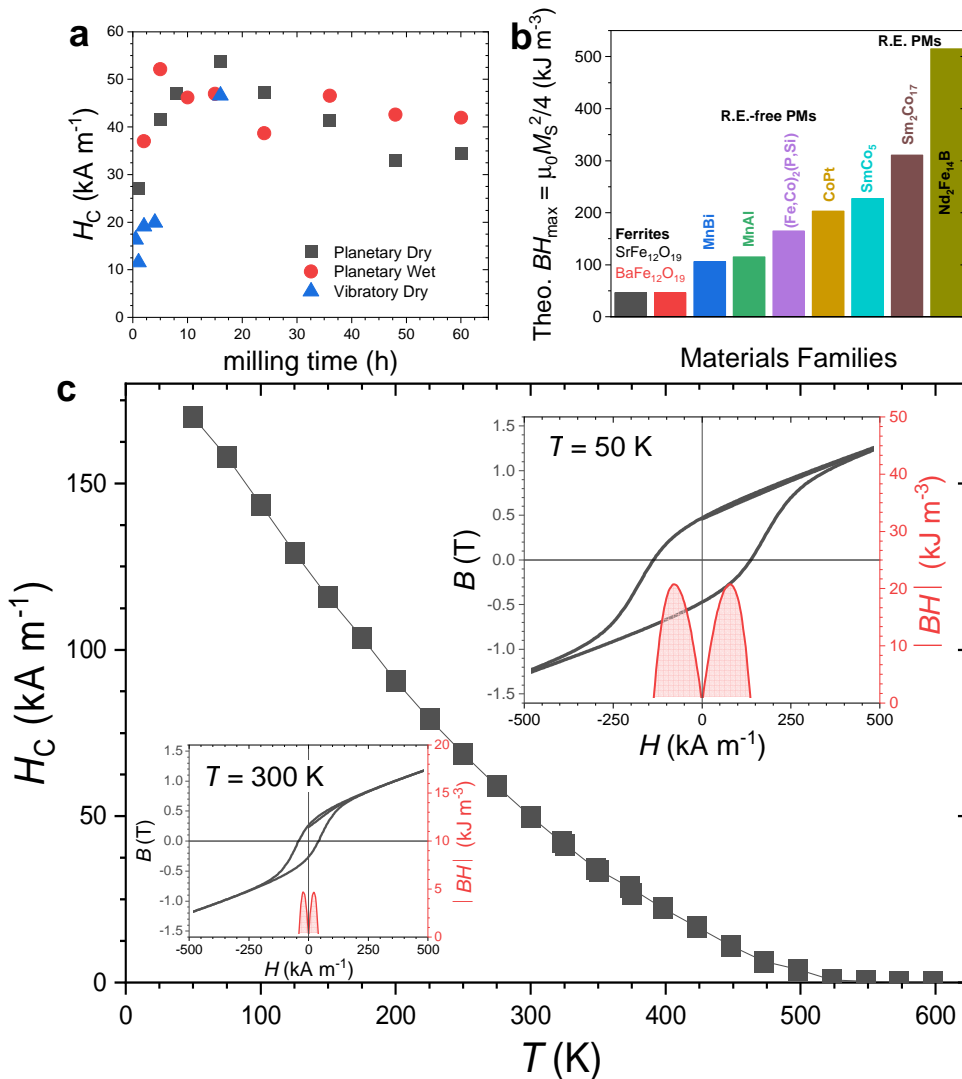
341 Although  $(\text{Fe},\text{Co})_2(\text{P},\text{Si})$  submicron-sized particles should be considered as a flammable solid, we  
 342 note that they are relatively stable. The presently reported particles were stored in a glovebox  
 343 employing a purified Ar atmosphere. But additional batches stored in air for a long period of time  
 344 (6 months) did not present a noticeable deterioration of their crystal structure, nor of their  
 345 magnetic properties.

### 346 3.4 Permanent magnetic properties of bounded $\text{Fe}_{2-y}\text{Co}_y\text{P}_{1-x}\text{Si}_x$ submicron-sized particles

347 Magnetization hysteresis cycles were recorded for  $\text{Fe}_{1.75}\text{Co}_{0.20}\text{P}_{0.75}\text{Si}_{0.25}$  submicron-sized particles  
 348 milled in different conditions and bonded with epoxy resin. **Figure 5** presents the evolution of the

349 coercive field as a function of the milling time for different milling conditions. The largest coercive  
350 fields are achieved for 8-16 h of milling. Additional magnetization cycles for 16 h milling (including  
351 the virgin magnetization curve) are shown in **Figure 6** and in Supplementary material. While  
352 coercive fields of  $\mu_0 H_c \approx 70$  mT ( $55 \text{ kA m}^{-1}$ ) at room temperature remain modest in comparison to  
353 rare-earth magnets, it clearly demonstrates that permanent magnetic properties can be obtained  
354 in  $(\text{Fe,Co})_2(\text{P,Si})$  quaternary alloys with the  $\text{Fe}_2\text{P}$ -type structure. ~~This shape is often considered  
355 as a signature of pinning-type coercivity [6,34], but is not a conclusive feature here as the samples  
356 might be formed of particles less than the critical size of a single domain. Two additional  
357 observations nevertheless suggest that pinning might be the dominant coercivity mechanism: *i*)  
358 coercivity is presently observed in ball-milled samples only, a technique known to cause in  
359 addition to surface stresses, large amount of structural and microstructural defects (vacancies  
360 and/or dislocations) which may act as pinning centers; *ii*)~~ The highest coercive field achieved so  
361 far in  $(\text{Fe,Co})_2(\text{P,Si})$  quaternary alloys ( $\mu_0 H_c \approx 0.14$  T, Supplementary material) was actually  
362 observed in  $\text{Fe}_{1.85}\text{Co}_{0.1}\text{P}_{0.6}\text{Si}_{0.4}$  particles showing a two phase mixture of  $\text{Fe}_2\text{P}$ -type and  
363 orthorhombic BCO-type structures. ~~, for which the significant secondary phase content can be  
364 expected to provide further pinning centers and enhance the coercivity.~~ The lower value of the  
365 room-temperature coercivity of  $\text{Fe}_{1.75}\text{Co}_{0.20}\text{P}_{0.75}\text{Si}_{0.25}$  submicron-sized particles compared to the  
366 value reported for  $\text{Fe}_{1.7}\text{Co}_{0.3}\text{P}$  powders ( $\mu_0 H_c \approx 0.2$  T [10]) primarily originates from the difference  
367 in synthesis methods, the lixiviating method yielding fine, relatively well dispersed, particles  
368 directly after leaching. Similarly ultrafine particles of  $(\text{Fe,Co})_2\text{P}$  ternary alloys (in the range 100 to  
369 20 nm) prepared by a gas phase reaction were found to reach a coercive field up to 0.32 T at  
370 room temperature [16]. When comparing  $\text{Fe}_{1.80}\text{Co}_{0.20}\text{P}$  ( $\mu_0 H_c \approx 30$  mT, Supplementary material)  
371 and  $\text{Fe}_{1.75}\text{Co}_{0.20}\text{P}_{0.75}\text{Si}_{0.25}$  submicrometric particles synthesized in similar conditions, the coercivity  
372 of the quaternary alloys is significantly larger. This confirms that: *(i)* quaternary  $(\text{Fe,Co})_2(\text{P,Si})$   
373 alloys are more promising for permanent magnets than ternary  $(\text{Fe,Co})_2\text{P}$  alloys and *(ii)* the  
374 optimal synthesis conditions maximizing the coercivity of ternary or quaternary alloys deriving

375 from  $\text{Fe}_2\text{P}$  have not yet been reached by the present top down ball-milling approach, so that a  
376 significant improvement of the coercivity is likely to be achievable. Recalling that the Sherrer's  
377 equation estimates the crystallite size and therefore tends to underestimate the real particle size  
378 and does not account for agglomeration during milling, our present particles do not have the  
379 optimal shape to reach the full potential of  $(\text{Fe,Co})_2(\text{P,Si})$  alloys for permanent magnetic  
380 applications. We can nevertheless note that  $(\text{Fe,Co})_2(\text{P,Si})$  quaternary alloys show higher Curie  
381 temperatures than  $(\text{Fe,Co})_2\text{P}$  ternary alloys [16,19] and therefore their permanent magnetic  
382 properties are preserved up to higher temperatures (up to about 480 K for the present sample,  
383 Figure 5).



384

385 **Figure 5.** Permanent magnetic properties of  $\text{Fe}_{1.75}\text{Co}_{0.20}\text{P}_{0.75}\text{Si}_{0.25}$  submicron-sized particles.

386 (a) Coercive field ( $H_c$ ) as a function of milling time for different milling conditions. (b) Theoretical

387  $|BH|_{\max}$  energy product estimated from the saturation magnetization for different families of

388 permanent magnets. (c) Temperature dependence of the coercive field for  $\text{Fe}_{1.75}\text{Co}_{0.20}\text{P}_{0.75}\text{Si}_{0.25}$

389 submicron-sized particles synthesized by 16 h of planetary ball milling (bonded oriented

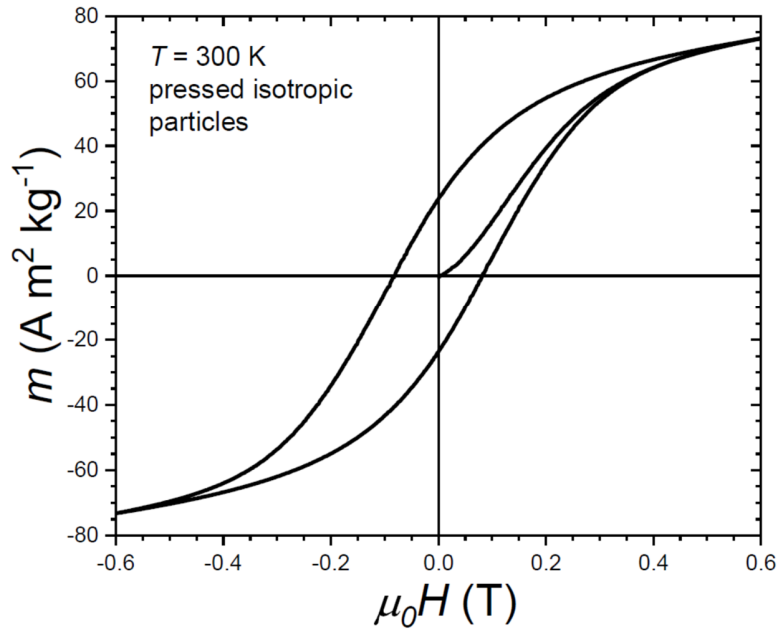
390 powders). The insets present the  $B(H)$  hysteresis measurements at 50 and 300 K.

391 When considering the theoretical  $|BH|_{\max}$ , which can be calculated from the saturation

392 magnetization as  $\mu_0 M_S^2/4 \approx 165 \text{ kJ m}^{-3}$  [6], we can see that  $(\text{Fe,Co})_2(\text{P,Si})$  materials are an

393 interesting intermediate between the high  $|BH|_{\max}$  of rare-earth magnets and the low performance  
394 of ferrites (Figure 5b). In particular, the theoretical  $|BH|_{\max}$  of  $(\text{Fe,Co})_2(\text{P,Si})$  is significantly larger  
395 (about +40%) than that of other candidates for rare-earth-free magnets, such as MnBi or MnAl.  
396 The experimental  $|BH|_{\max}$  obtained in the present  $\text{Fe}_{1.75}\text{Co}_{0.20}\text{P}_{0.75}\text{Si}_{0.25}$  submicrometric particles  
397 bonded by epoxy resin and oriented in a  $\mu_0 H = 1.1$  T magnetic field range from about  $21 \text{ kJ m}^{-3}$   
398 at 50 K (~12% of the theoretical  $|BH|_{\max}$ ) to about  $5 \text{ kJ m}^{-3}$  at room temperature. These energy  
399 products are still small compared to the theoretical ones or compared to the well-established  
400 permanent magnetic materials. These low performances are partially due to the imperfect  
401 orientation process, the energy products for the oriented bonded samples were found to be only  
402 ~20% higher than the corresponding isotropic bonded sample, which may be due to particles  
403 agglomeration during milling. But they are already comparable to that of ferrite magnets (of the  
404 order of  $15 \text{ kJ m}^{-3}$  for oriented bonded ferrites and  $5 \text{ kJ m}^{-3}$  for isotropic bonded ferrites) [6]. The  
405 magnetic hardness parameters obtained in section 3.2 ( $\kappa \approx 1.3$ ) settles  $(\text{Fe,Co})_2(\text{P,Si})$  amongst  
406 hard magnetic materials, for which a more significant fraction of the theoretical  $|BH|_{\max}$  should be  
407 achievable. It often takes a long struggle from the introduction of a new hard magnetic composition  
408 to reach its full potential as permanent magnet. As mentioned above for the coercive field,  
409 significant improvements of the experimental  $|BH|_{\max}$  can be expected by optimizing the material  
410 synthesis and magnet preparation conditions.





411

412

413

414

415

**Figure 6.** Magnetization cycle including the initial magnetization branch at  $T = 300$  K of isotropically pressed  $\text{Fe}_{1.75}\text{Co}_{0.20}\text{P}_{0.75}\text{Si}_{0.25}$  submicron-sized particles prepared by 16 h dry milling.

#### 4. Conclusions

416

417

418

419

420

421

422

423

424

425

Ternary  $(\text{Fe,Co})_2\text{P}$  and quaternary  $(\text{Fe,Co})_2(\text{P,Si})$  alloys were successfully prepared in single crystal form and their magnetic properties were investigated. Compared to the binary parent  $\text{Fe}_2\text{P}$ , substitutions with Co or Si decrease the magneto-crystalline anisotropy at low temperature, but increase the Curie temperature. As a result, the magneto-crystalline anisotropy at room temperature is enhanced in  $(\text{Fe,Co})_2(\text{P,Si})$  quaternary alloys. The present  $\text{Fe}_{1.94}\text{Co}_{0.10}\text{P}_{0.61}\text{Si}_{0.33}$  single crystal shows the largest magneto-crystalline anisotropy of  $K_1 \approx 0.9 \text{ MJ m}^{-3}$  at room temperature, which brings support to former preliminary polycrystalline data, and confirms that  $(\text{Fe,Co})_2(\text{P,Si})$  show a much stronger magnetic anisotropy than ferrites.  $(\text{Fe,Co})_2(\text{P,Si})$  submicron-sized particles were synthesized by a top-down ball-milling approach and their magnetization was recorded. For the first time, hard magnetic properties were observed in  $(\text{Fe,Co})_2(\text{P,Si})$  quaternary

426 alloys. While the coercive field and energy products are nearly comparable with ferrites, they so  
427 far remain modest in comparison to other well-established permanent magnetic materials. Yet  
428 further improvements of the performances are anticipated by optimization of the synthesis  
429 conditions. Owing to the high economical interest that a permanent magnet essentially made of  
430 iron and abundant metalloid elements has,  $(\text{Fe,Co})_2(\text{P,Si})$  quaternary alloys are promising rare-  
431 earth-free permanent magnet materials that deserve further investigation.

432

### 433 **Acknowledgments**

434 The work is supported by the Inner Mongolia Normal University (grant numbers 2018YJRC002  
435 and 2018YJRC003), the Inner Mongolia Autonomous Region (grant numbers NJZY20025 and  
436 NJYT-20-A17) and the National Natural Science Foundation of China (grant numbers 11904188  
437 and 51961033).

438

### 439 **References**

- 440 [1] J. M. D. Coey, Perspective and Prospects for Rare Earth Permanent Magnets, *Engineering*  
441 2020, 6, 119-131.
- 442 [2] O. Gutfleisch, M. A. Willard, E.Brück, C. H. Chen, S. G. Sankar, J. P. Liu, *Magnetic Materials*  
443 and Devices for the 21st Century: Stronger, Lighter, and More Energy Efficient, *Adv. Mater.*  
444 2011, 23, 821-842.
- 445 [3] J. Cui, M. Kramer, L. Zhou, F. Liu, A. Gabay, G. Hadjipanayis, B. Balasubramanian, D.  
446 Sellmyer, Current Progress and Future Challenges in rare-earth-free Permanent Magnets, *Acta*  
447 *Mater.* 2018, 158, 118-137.
- 448 [4] J. M. D. Coey, Permanent magnets: Plugging the gap, *Scripta Mater.* 2012, 67, 524-529.

- 449 [5] A. K. Pathak, M. Khan, K. A. Gschneidner Jr., R. W. McCallum, L. Zhou, K. Sun, K. W.  
450 Dennis, C. Zhou, F. E. Pinkerton, M. J. Kramer, V. K. Pecharsky, Cerium: An Unlikely  
451 Replacement of Dysprosium in High Performance Nd–Fe–B Permanent Magnets, *Adv. Mater.*  
452 2015, 27, 2663-2667.
- 453 [6] J. M. D. Coey, *Magnetism and Magnetic Materials*, Cambridge University Press, Cambridge,  
454 UK, 2019.
- 455 [7] H. Fujii, T. Hokabe, T. Kamigaichi, T. Okamoto, Magnetic Properties of Fe<sub>2</sub>P Single Crystal,  
456 *J. Phys. Soc. Jpn.* 1977, 43, 41-46.
- 457 [8] L. Lundgren, G. Tarmohamed, O. Beckman, B. Carlsson, S. Rundqvist, First Order Magnetic  
458 Phase Transition in Fe<sub>2</sub>P, *Phys. Scripta* 1978, 17, 39-48.
- 459 [9] L. Caron, M. Hudl, V. Höglin, N. H. Dung, C. P. Gomez, M. Sahlberg, E. Brück, Y.  
460 Andersson, P. Nordblad, Magnetocrystalline Anisotropy and the Magnetocaloric Effect in Fe<sub>2</sub>P,  
461 *Phys. Rev. B* 2013, 88, 094440.
- 462 [10] K. J. de Vos, W. A. J. J. Velge, M. G. van der Steeg, H. Zijlstra, Permanent Magnetic  
463 Properties of Iron - Cobalt - Phosphides, *J. Appl. Phys.* 1962, 33, 1320-1322.
- 464 [11] R. Fruchart, A. Roger, J. P. Senateur, Crystallographic and Magnetic Properties of Solid  
465 Solutions of the Phosphides M<sub>2</sub>P, M = Cr, Mn, Fe, Co, and Ni, *J. Appl. Phys.* 1969, 40, 1250-  
466 1257.
- 467 [12] H. Fujii, T. Hokabe, T. Kamigaichi, H. Fujiwara, T. Okamoto, Magnetic Properties of Single  
468 Crystals of the System (Fe<sub>1-x</sub>Ni<sub>x</sub>)<sub>2</sub>P, *J. Phys. Soc. Jpn.* 1978, 44, 96-100.
- 469 [13] R. Chandra, S. Bjarman, T. Ericsson, L. Häggström, C. Wilkinson, R. A. Wäppling,  
470 Mössbauer and X-ray Study of Fe<sub>2</sub>P<sub>1-x</sub>B<sub>x</sub> Compounds (x < 0.15), *J. Solid State Chem.* 1980, 34,  
471 389-396.

- 472 [14] P. Jernberg, A. A. Yousif, L. Häggström, Y. Andersson, A Mössbauer study of  $\text{Fe}_2\text{P}_{1-x}\text{Si}_x$  ( $x$   
473  $\leq 0.35$ ), *J. Solid State Chem.* 1984, 53, 313-322.
- 474 [15] A. Catalano, R. J. Arnott, A. Wold, Magnetic and Crystallographic Properties of the System  
475  $\text{Fe}_2\text{P}_{1-x}\text{As}_x$ , *J. Solid State Chem.* 1973, 7, 262-268.
- 476 [16] Y. Tokuoka, J. Yoshinari, Ferromagnetic ultrafine Particles, Method of Making, and  
477 Recording Medium using the same. US patent US005256479A, 1993.
- 478 [17] A. Mendoza-Garcia, H. Zhu, Y. Yu, Q. Li, L. Zhou, D. Su, M. J. Kramer, S. Sun, Controlled  
479 Anisotropic Growth of Co-Fe-P from Co-Fe-O Nanoparticles, *Angew. Chem. Int. Ed.* 2015, 54,  
480 9642.
- 481 [18] W. Yang, X. Wu, Y. Yu, C. Yang, S. Xu, H. Li, Controlled Synthesis and Magnetic  
482 Properties of Iron–Cobalt–Phosphide Nanorods, *Nanoscale* 2016, 8, 16187-16191.
- 483 [19] D. Li, M. P. Arachchige, B. Kulikowski, G. Lawes, T. Seda, S. L. Brock, Control of  
484 Composition and Size in Discrete  $\text{Co}_x\text{Fe}_{2-x}\text{P}$  Nanoparticles: Consequences for Magnetic  
485 Properties, *Chem. Mater.* 2016, 28, 3920-3927.
- 486 [20] E. K. Delczeg-Czirjak, Z. Gercsi, L. Bergqvist, O. Eriksson, L. Szunyogh, P. Nordblad, B.  
487 Johansson, L. Vitos, Magnetic Exchange Interactions in B-, Si-, and As-doped  $\text{Fe}_2\text{P}$  from First-  
488 Principles Theory, *Phys. Rev. B* 2012, 85, 224435.
- 489 [21] M. Costa, O. Grånäs, A. Bergman, P. Venezuela, P. Nordblad, M. Klintonberg, O. Eriksson,  
490 Large Magnetic Anisotropy of  $\text{Fe}_2\text{P}$  Investigated via ab initio Density Functional Theory  
491 Calculations, *Phys. Rev. B* 2012, 86, 085125.
- 492 [22] I. A. Zhuravlev, V. P. Antropov, A. Vishina, M. van Schilfgaarde, K. D. Belashchenko,  
493 Tunable Dimensional Crossover and Magnetocrystalline Anisotropy in  $\text{Fe}_2\text{P}$ -based Alloys, *Phys.*  
494 *Rev. Materials* 2017, 1, 051401(R).

495 [23] O. Tegus, E. Brück, K. H. J. Buschow, F. R. de Boer, Transition-metal-based magnetic  
496 refrigerants for room-temperature applications, *Nature* 415 (2002) 150–152.

497 [24] D. Liu, M. Yue, J. Zhang, T. M. McQueen, J. W. Lynn, X. Wang, Y. Chen, J. Li, R. J. Cava,  
498 X. Liu, Z. Altounian, Q. Huang, Origin and tuning of the magnetocaloric effect in the magnetic  
499 refrigerant  $Mn_{1.1}Fe_{0.9}(P_{0.8}Ge_{0.2})$ , *Phys. Rev. B* 79 (2009) 014435.

500 [25] N. H. Dung, Z.Q. Ou, L. Caron, L. Zhang, D.T. Cam Thanh, G.A. de Wijs, R.A. de Groot,  
501 K.H.J. Bushow, E. Brück, *Mixed Magnetism for Refrigeration and Energy Conversion*, *Adv.*  
502 *Energy Mater.* 1 (2011) 1215–1219.

503 [26] M. Fries, L. Pfeuffer, E. Bruder, T. Gottschall, S. Ener, L. V. B. Diop, T. Gröb, K. P. Skokov,  
504 O. Gutfleisch, Microstructural and magnetic properties of Mn-Fe-P-Si (Fe<sub>2</sub> P-type)  
505 magnetocaloric compounds, *Acta Materialia* 132 (2017) 222-229.

506 [27] F. Guillou, Sun-Liting, O. Haschuloo, Z. Q. Ou, E. Brück, O. Tegus, H. Yibole, Room  
507 Temperature Magnetic Anisotropy in Fe<sub>2</sub>P-Type Transition Metal Based Alloys, *J. Alloys*  
508 *Compd.* 2019, 800, 403-411.

509 [28] J. Y. Xu, Lingling-Bao, H. Yibole, F. Guillou, Structure and Magnetic Properties of  
510  $Fe_{1.95-x}Ni_xP_{1-y}Si_y$  Alloys, *Solid State Commun.* 2020, 319, 113996.

511 [29] H. Yibole, F. Guillou, Y. K. Huang, G. R. Blake, A. J. E. Lefering, N. H. van Dijk, E. Brück,  
512 First-order Ferromagnetic Transition in Single-crystalline (Mn,Fe)<sub>2</sub>(P,Si), *Appl. Phys. Lett.* 2015,  
513 107, 162403.

514 [30] J. Rodríguez-Carvajal, Recent Advances in Magnetic Structure Determination by Neutron  
515 Powder Diffraction, *Physica B: Condens. Matter* 1993, 192, 55-69.

516 [31] K. Momma, F. Izumi, VESTA 3 for three-dimensional visualization of crystal, volumetric and  
517 morphology data, *J. Appl. Crystallogr.* 2011, 44, 1272-1276.

- 518 [32] E. R. Callen and H. B. Callen, Anisotropic Magnetization, *J. Phys. Chem. Solids* 1960, 16,  
519 310.
- 520 [33] W. Sucksmith, F. R. S. Thompson, J. E. Thompson, The Magnetic Anisotropy of Cobalt,  
521 *Proc. Royal Soc. A* 1954, 225, 362-375.
- 522 [34] É. du Trémolet de Lacheisserie, D. Gignoux, M. Schlenker, *Magnetism*, Springer, New  
523 York, NY, 2005.
- 524 [35] R. Skomski, J. M. D. Coey, Magnetic anisotropy — How much is enough for a permanent  
525 magnet? *Scripta Mater.* 2016, 112, 3-8.
- 526 [36] J. Wang, F. Zhao, W. Wu, G. M. Zhao, Unusual Temperature Dependence of the Magnetic  
527 Anisotropy Constant in Barium Ferrite  $\text{BaFe}_{12}\text{O}_{19}$ , *J. Appl. Phys.* 2011, 110, 096107.
- 528 [37] R. C. Pullar, Hexagonal Ferrites: a Review of the Synthesis, Properties and Applications of  
529 Hexaferrite Ceramics, *Prog. Mater. Sci.* 2012, 57, 1191-1334.
- 530 [38] B. W. Roberts, Neutron Diffraction Study of the Structures and Magnetic Properties of  
531 Manganese Bismuthide, *Phys. Rev.* 1956, 104, 607.
- 532 [39] L. Pareti, F. Bolzoni, F. Leccabue, A. E. Ermakov, Magnetic Anisotropy of MnAl and MnAlC  
533 Permanent Magnet Materials, *J. Appl. Phys.* 1986, 59, 3824.
- 534 [40] H. Shima, K. Oikawa, A. Fujita, K. Fukamichi, K. Ishida, S. Nakamura, T. Nojima,  
535 Magnetocrystalline Anisotropy Energy in L10-type CoPt Single Crystals, *J. Magn. Magn. Mater.*  
536 2005, 290–291, 566-569.
- 537 [41] K. Inoue, H. Shima, A. Fujita, K. Ishida, K. Oikawa, K. Fukamichi, Temperature  
538 Dependence of Magnetocrystalline Anisotropy Constants in the Single Variant State of L10-  
539 Type FePt Bulk Single Crystal, *Appl. Phys. Lett.* 2006, 88, 102503.

540 [42] N. V. Thang, N. H. van Dijk, E. Brück, Effects of Milling Conditions on Nano-scale  
541 MnFe(P,Si) Particles by Surfactant-assisted High-energy Ball Milling, Phys. Procedia 2015, 75,  
542 1104-1111.